Earth and Planetary Science Letters 432 (2015) 95–102

Contents lists available at ScienceDirect

Earth and Planetary Science Letters

www.elsevier.com/locate/epsl

The work of fault growth in laboratory sandbox experiments

Justin W. Herbert [a,*], Michele L. Cooke [a], Pauline Souloumiac [b], Elizabeth H. Madden [a], Baptiste C.L. Mary [b], Bertrand Maillot [b]

[a] Department of Geosciences, University of Massachusetts Amherst, 611 North Pleasant Street, Amherst, MA 01003-9297, United States
[b] Département Géosciences et Environnement, Université de Cergy-Pontoise, Cergy-Pontoise F-95000, France

ARTICLE INFO

Article history:
Received 7 February 2015
Received in revised form 19 September 2015
Accepted 26 September 2015
Available online 3 November 2015
Editor: A. Yin

Keywords:
work budget
fault growth
analog sandbox experiments

ABSTRACT

Contractional sandbox experiments that simulate crustal accretion and direct shear tests both provide direct data on the amount of work required to create faults (W_{prop}) in granular materials. Measurements of force changes associated with faulting reveal the work consumed by fault growth, which can be used to predict fault growth path and timing. Within the contractional experiments, the sequence and style of early faulting is consistent for the range of sand pack thicknesses tested, from 12 to 30 mm. Contrary to expectations that W_{prop} is only a material property, the experimental data show that for the same material, W_{prop} increases with sand pack thickness. This normal stress dependence stems from the frictional nature of granular materials. With the same static and sliding friction values, incipient faults initiated deeper in the sand pack have larger shear stress drops, due to increased normal compression, σ_n. For CV32 sand, the relationship between W_{prop} and σ_n, calculated from the force drop data as W_{prop} (J/m^2) $= 2.0 \times 10^{-4}$ (m) σ_n (Pa), is consistent with the relationship calculated from direct shear test data as W_{prop} (J/m^2) $= 2.4 \times 10^{-4}$ (m) σ_n (Pa). Testing of different materials within the contractional sandbox (fine sand and glass beads) shows the sensitivity of W_{prop} to material properties. Both material properties and normal stress should be considered in calculations of the work consumed by fault growth in both analog experiments and crustal fault systems.

© 2015 Elsevier B.V. All rights reserved.

1. Introduction

The concept of a balanced energy budget has been widely applied in the Earth sciences to study geologic structures and tectonic deformation, usually following a work minimization approach (e.g., Cooke and Madden, 2014). This approach derives directly from the work of Griffith (1920), who showed that, for a system at equilibrium, the energy required for crack growth is matched by an equal and opposite change in the system's total mechanical energy. Irwin (1958) used Griffith's energy balance to define the critical energy release rate, which relates the energy required to grow a crack to the critical stress intensity factors, the stress magnitudes required for fracture propagation. Critical stress intensity factors (i.e., fracture toughness for mode I) are considered properties of the material containing the crack and are therefore independent of a crack's size, orientation relative to remote loading, and the tractions along the failure surface. Consequently, the critical energy release rate predicts that fault growth consumes the same work regardless of depth in the crust.

The critical energy release rate has been successful in describing co-linear sliding-crack propagation in ductile materials; however, the few empirical measures of the critical values required for mode II and III crack growth in rock provide inconsistent results. Many laboratory experiments and field measurements have estimated the work consumed during fault growth by accurately measuring the total area of new surfaces created (e.g., Wong, 1982; Chester et al., 2005; Wilson et al., 2005). The total work is that area times the specific surface energy for minerals, typically ~1 J/m^2 (e.g., Brace and Walsh, 1962). Estimates from laboratory experiments return a wide range of values from 10^1 to 10^4 J/m^2 (e.g., Wong, 1982; Ohnaka et al., 1997; Cox and Scholz, 1988; Kato et al., 2003). Meanwhile, field estimates from mining-induced earthquakes, pseudotachylyte formation for a single fault slip event, and fault gouge development produce values an orders of magnitude greater, ranging from 10^5 to 10^6 J/m^2 (e.g., Olgaard and Brace, 1983; Chester et al., 2005; Wilson et al., 2005; Pittarello et al., 2008).

Failure according to the Coulomb criterion (e.g., Jaeger et al., 2007) differs from the energy release approach, in that Coulomb failure depends not only on the material properties of inherent

* Corresponding author. Now at Chevron ETC, 1500 Louisiana, Houston, TX 77002, United States.
E-mail address: jherbert@geo.umass.edu (J.W. Herbert).

http://dx.doi.org/10.1016/j.epsl.2015.09.046
0012-821X/© 2015 Elsevier B.V. All rights reserved.

shear strength and the coefficient of internal friction, but also on the normal stress resolved on the potential failure plane. This normal stress dependence means that higher shear stress is required to overcome higher normal stresses on incipient faults deeper in the Earth. There are some drawbacks to using the Coulomb failure criterion to model fault growth. The orientation of the maximum Coulomb stress predicts the orientation of new shear surfaces, but results in two potential failure surfaces for a given stress condition, which adds ambiguity to fault prediction. In addition, fault growth within analog experiments does not always occur where the Coulomb stresses are greatest (e.g., Del Castello and Cooke, 2007). In contrast to the Coulomb failure criterion, prediction of fault propagation path via work minimization shows that faults grow in the singular orientation that provides the highest work savings (e.g., Cooke and Murphy, 2004; Del Castello and Cooke, 2007; Cooke and Madden, 2014). This approach finds only one orientation for shear failure, and simultaneously accounts for the possibility of growth by tensile failure (Cooke and Madden, 2014).

The direct calculation of the work required to grow faults within contractional sandbox models and direct shear tests presented here provides further insight into the timing and path of fault growth. For centuries, analog models have been used to investigate fault evolution on both length and time scales suitable for easily repeatable laboratory experiments (e.g., Hall, 1815; Graveleau et al., 2012). Utilizing controlled applied displacements and properly scaled material properties (e.g., Hubbert, 1937), analog models provide quantitative data of fault system evolution, including the evolving displacement field and the total backwall force required to deform the sand body. Sandbox rigs that measure stress in situ (Nieuwland et al., 2001) or along their moving wall (Cruz et al., 2010; Cubas et al., 2010; Souloumiac et al., 2012) permit direct observations of the work consumed during fault growth. Similarly, direct shear tests record the evolution of shear stress during fault formation (e.g. Lohrmann et al., 2003; Panien et al., 2006; Maillot, 2013), which can be used to estimate work of fault growth.

We determine the work required to grow faults within contractional sandbox analog experiments conducted at the Université de Cergy-Pontoise (UCP) from changes in backwall force associated with fault growth. We also use measurements from direct shear tests performed by Maillot (2013) with a Casagrande shear box to provide an independent estimate of the work of fault growth. We demonstrate that sandbox and Casagrande shear box tests allow for estimates of the work required to grow faults in sand, which are useful for predicting the timing and path of fault growth. Estimates from experiments with different sand layer thicknesses and direct shear stress under different normal load highlight the dependency of the work of fault growth on normal stress.

2. Work of fault growth

The work required to grow faults is one component of a fault system work budget. The complete deformational work budget consists of five components: internal work, W_{int}, work against gravity, W_{grav}, work against friction, W_{fric}, seismic radiated energy, W_{seis}, and the work of fault propagation, W_{prop} (e.g., Hardy et al., 1998; Masek and Duncan, 1998; Cooke and Murphy, 2004; Del Castello and Cooke, 2007; Savage and Cooke, 2010; Dempsey et al., 2012; Cooke and Madden, 2014; Yagupsky et al., 2014). These components sum to the total external work, W_{ext}, applied to the system:

$$W_{ext} = W_{int} + W_{grav} + W_{fric} + W_{prop} + W_{seis} \quad (1)$$

During an episode of fault growth, potential energy stored in the system as work against gravity (W_{grav}) and strain energy within the host rock (W_{int}) is released as frictional heating (W_{fric}), seismic energy (W_{seis}), and energy to break the rock (W_{prop}). Thus, W_{fric}, W_{seis} and W_{prop} are non-recoverable and lost to the system. Within sand experiments, faulting is stable and only a very small amount of energy is released as acoustic energy, W_{seis}. W_{fric} is related to the fault strength during stable sliding and the total slip along the fault, while W_{prop} is related to the evolution of shear stress during the onset of faulting (Fig. 1A). As fault growth occurs and the new fault slips through the slip weakening distance, L, the shear stress drops from the peak stress value, equivalent to the strength of the material, to a sliding shear stress. Within granular materials, slip weakening is associated with dilation and rearrangement of grains at the onset of failure (Lohrmann et al., 2003; Panien et al., 2006). Direct shear tests record the evolution of shear stress with onset of faulting (e.g. Lohrmann et al., 2003; Panien et al., 2006; Maillot, 2013) from which W_{prop} can be estimated as the area under the shear stress versus slip curve that lies above the sliding shear stress (Fig. 1A). For our estimates, we use the experimental results of Maillot (2013) that use identical sand to that within the contractional experiments, where the work of fault growth is estimated from the changes in W_{ext} on the system.

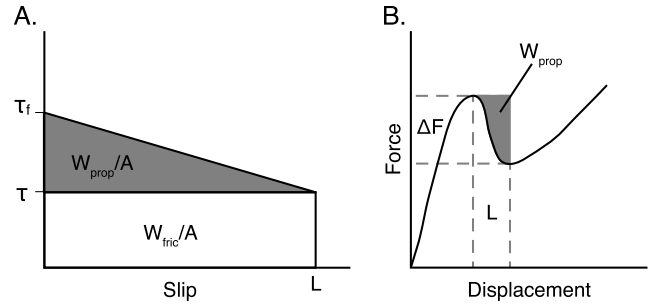

Fig. 1. A) During fault slip the partitioning of energy also includes work of frictional resistance per fault area (W_{fric}/A). τ_f is the shear strength at failure, τ is the shear strength during sliding and L is the sliding distance over which the stress drop from τ_f to τ takes place (eq. (1)). B) Schematic representation of a force–displacement curve showing a faulting event and the resulting change in force over a backwall displacement during fault growth. W_{prop} equals the work lost during the faulting event.

At the onset of fault growth within the contractional experiments, W_{prop} equals the change in W_{ext}, ΔW_{ext} (Fig. 1B). Using the data from the sandbox experiments, W_{prop} is calculated as one-half of the product of the change in force measured on the backwall, ΔF, and the slip weakening distance over which the force drop takes place, L:

$$W_{prop} = \Delta W_{ext} = \frac{1}{2}\Delta F L \quad (2)$$

ΔF is measured from peak to trough in the force time series (Fig. 1A). The total force to displace the experiment over the interval of fault growth is due to W_{fric} as well as W_{int} and W_{grav}. All of these work components change during the interval of fault growth to produce a more efficient system that deforms under lower force. Specifically, the W_{fric} along new accretion faults is less than that along older faults that have greater overburden weight (Del Castello and Cooke, 2007). The magnitude of the drop in W_{ext} associated with faulting reflects the work consumed by weakening associated with fault growth. The system could attain a more efficient fault configuration at any time but cannot do so until the work required to grow the fault can be provided by the work savings of the more efficient system, $\Delta W_{ext} = W_{prop}$ (Del Castello and Cooke, 2007). Furthermore, Cooke and Madden (2014) demonstrate that, when the stresses meet the empirically derived strength measurements, the energy required for growth is equivalent to the change in W_{ext}.

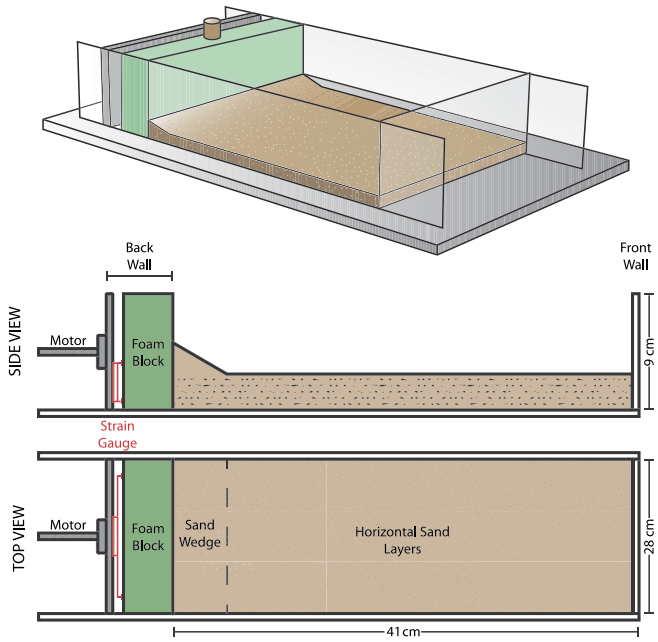

Fig. 2. Oblique, side, and top view of the experimental set-up. Backwall is translated from left to right toward the frontwall by the electric screw motor.

While the direct shear tests provide a controlled set up for recording the onset of faulting, the normal stresses applied to the shear tests exceed those resolved on low angle fault surfaces within the contractional experiments. Tracking the evolution of W_{ext} on the contraction experiments during the onset of faulting provides a way to estimate work of fault growth within a system where faults self-organize and are not constrained. By using both approaches, we provide independent analyses of the work consumed by fault growth in the granular material used to simulate crustal deformation.

3. Contractional sandbox modeling

We analyze data from contractional sandbox wedge experiments performed at UCP that use coarse grain sand, fine grain sand, or spherical glass beads. Continuous measurements of the moving wall force, in combination with overhead and side photographs, record deformation throughout experiments.

3.1. Deformation sandbox

The sandbox (Fig. 2) is a rectangular shear box with inside dimensions of 41 cm in length and 28 cm in width. The frontwall, basal plate, and sidewalls of the sandbox are made of 1 cm thick glass and fixed in position (i.e., an indentation style sandbox). The basal plate of the model has a slope of 0°. An electric screw motor translates the backwall toward the frontwall at constant speed. Although the rate of backwall displacement varies between experiments (Table 1), deformation is not affected over this range; the pattern of deformation and shape of the force-displacement curves at different speeds are consistent. The backwall consists of a foam block backed with strain gauges that record strain every 0.1 s (Fig. 2). The foam block resists tilting and an added weight keeps the block in contact with the base of the sandbox. The strain gauges exhibit a known linear-elastic behavior, allowing backwall measurements of strain to be converted to force (Cubas et al., 2010). In addition to the strain gauges, two cameras capture overhead and side photographs every 5 s. Particle Image Velocimetry (PIV) aids in the analysis of deformation within sand packs by providing the instantaneous velocity of sand grains through correlation of pixel constellations between successive images (e.g., Adam et al., 2005; Hoth, 2005). Where the foam block comes in contact with glass, both along the bottom and sides of the box, Teflon and felt reduce friction and prevent sand from becoming entrained between the foam block and glass plates. The indentation style sandbox minimizes sidewall friction, which skews the results captured by the side camera (Souloumiac et al., 2012). Additionally, the sidewalls are treated with Rain-X and buffed prior to each experiment to further reduce the sidewall friction coefficient from ∼0.27 to ∼0.19 (Cubas et al., 2013), further reducing skewed results along the viewing glass.

Table 1
Experimental parameters. The height of the horizontal sand pack and speed of the backwall displacement varied among experiments.

Experiment number	Granular material	Height (mm)	Speed (mm/s)
189	CV32	20	0.47
221	CV32	14	0.94
222	CV32	12	0.47
223	CV32	11	0.22
224	CV32	13.5	0.22
240	CV32	16	0.22
241	CV32	14	0.22
272	CV32	12	0.22
253	GA39	14	0.22
254	glass beads	14	0.22
309	CV32	30	0.22

In the experiments, the horizontal layer thickness is varied from 11 to 30 mm (Table 1). The material emplacement technique can greatly affect the frictional coefficient of granular materials (Krantz, 1991; Lohrmann et al., 2003; Panien et al., 2006; Maillot, 2013). Sifting granular material is preferred over pouring, because sifting creates reproducible, planar, homogeneous, and dense layers (Krantz, 1991; Cubas et al., 2010; Maillot, 2013). The sand layers of the experiments are emplaced with a multi-sieved sedimentation device, where material released from a reservoir above the sandbox passes through two or three sieves before settling in the box (Maillot, 2013). Prior to deformation, a small protowedge is added on top of the sand layer in front of the moving wall. The slope of the protowedge equals the granular material's angle of repose. The protowedge focuses the onset of deformation at the toe of the protowedge, away from the moving wall, and facilitates a consistent sequence of initial faulting between experiments.

3.2. Material properties

The granular material tested is either Fontainebleau aeolian quartz sand of type CV32 or GA39, or glass beads. First, we present detailed results for the experiments with CV32, a coarse grain sand with a median grain size of 250 μm that is poorly-sorted and has a density of 1711 ± 7 kg/m^3 (Cubas et al., 2010; Maillot, 2013). Then, we compare these results with those from experiments with GA39 and with glass beads. GA39 is a fine grain sand with a median grain size of 90 μm that is well sorted and has a density of 1543 ± 20 kg/m^3 (Maillot, 2013). The glass beads have a median grain size of 160 μm and a density of 1573 ± 7 kg/m^3.

Maillot (2013) measured the static and dynamic frictional properties of the sand using a Casagrande shear device and the same sedimentation device used here. The Casagrande shear box consists of a mobile lower half, which is displaced with a stepwise motor, and a fixed upper half, which is held in position by a force that is measured throughout the experiment. The CV32 drops from peak internal friction of 0.96 at failure to dynamic sliding friction of 0.72 over a slip distance of ∼2 mm (Maillot, 2013). Slip weakening frictional properties for GA39 and the glass beads used in these

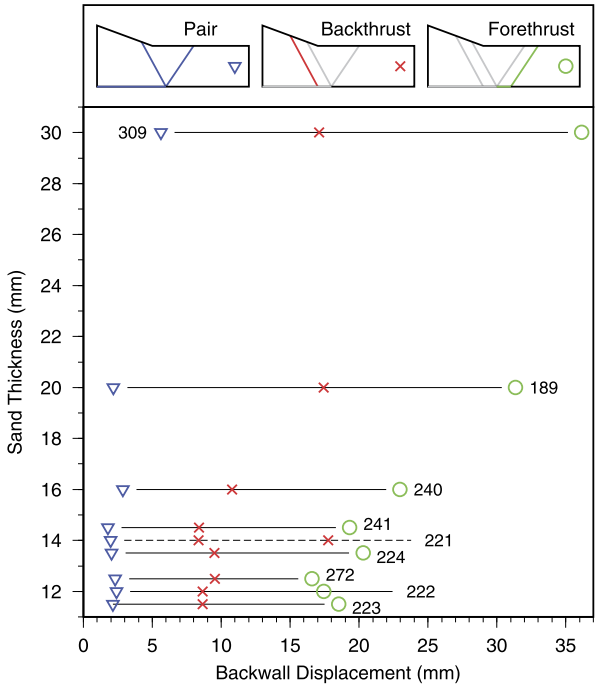

Fig. 3. Timing of first three faults to develop within the sandbox for various depths of CV32 sand. Inset at top shows the geometry of these faults. Experiments are summarized in Table 1. With the exception of 221 (dotted line), a forethrust–backthrust pair develops first, then a backthrust, followed by a forethrust. Errors in displacement at onset of faulting are <1 mm.

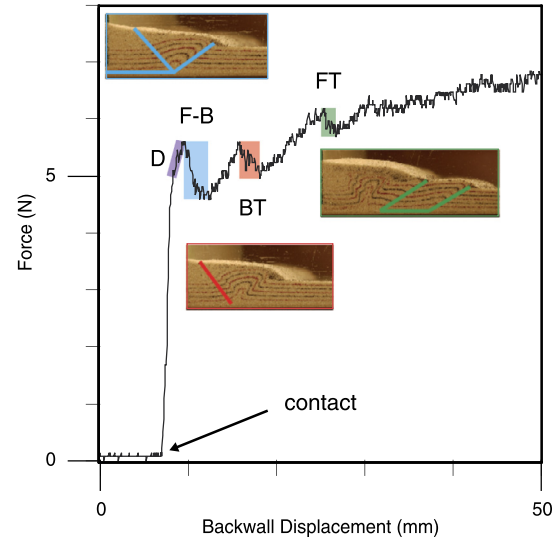

Fig. 4. Force–displacement data for experiment 222. After the strain gauges make contact with the foam block, the force increases until the first faulting event, a forethrust–backthrust pair (blue highlighted area). The region D (purple highlighted area), shows the timing of slip along the detachment and compaction of the sand wedge. Elastic loading occurs between the timing of first contact and D. The forethrust–backthrust pair forms during the backwall displacement from peak to trough and then the force increases until the next faulting event. The second fault is a backthrust (red highlighted area) and the third faulting event includes a pair of forethrusts (green highlighted area). (For interpretation of the references to color in this figure legend, the reader is referred to the web version of this article.)

experiments are not yet available. Panien et al. (2006) report static and dynamic frictions of 0.41 and 0.38 for similar glass beads. The analysis from this study provides qualitative comparisons of relative W_{prop} for the different materials.

4. Results

In the sandbox, new accretionary faults develop in response to the convergent backwall displacement. Two types of faults form to thicken or lengthen the wedge: 1) detachment faults form at the interface of the sand pack and basal plate, and 2) ramp thrusts form within the sand pack. Ramp faults dip either towards the moving wall as forethrusts or towards the toe of the wedge as backthrusts, and can occur as a forethrust–backthrust pair or individually (Fig. 3 inset). Drops in backwall force during fault growth can be attributed to the fault system acquiring a more efficient configuration that requires less force to accommodate the backwall displacement. Force drops associated with fault growth are recorded for 46 faulting events within nine experiments. We use eq. (2) to calculate W_{prop} for each faulting event from the associated force drops and backwall displacements. First, we present detailed results for the experiments with the coarse grain sand, CV32. Then, we calculate W_{prop} using strength data from six Casagrande shear box experiments performed by Maillot (2013), and compare these estimates with those from the sandbox experiments. This shows the consistent dependence of W_{prop} on normal stress across both sets of experiments. We also highlight the dependence of W_{prop} on material properties by presenting results from experiments with the fine grain sand, GA39, and with glass beads.

4.1. Sequence of faulting in experiments

The sequence of the first three episodes of faulting is consistent within all CV32 experiments. This is shown in Fig. 3, which differentiates the experiments by sand pack thickness. Initially, at backwall displacements of less than ∼5 mm, the detachment slips ahead of the wedge, then a forethrust–backthrust pair develops. A single out-of-sequence backthrust forms next, between the backwall and forethrust–backthrust pair, between 7 and 20 mm of backwall displacement. In most of the experiments, this is followed by slip along the detachment and the growth of a forethrust within the undisturbed sand pack ahead of the wedge, between 15 and 27 mm of backwall displacement. With continued convergence, a new forethrust–backthrust pair and individual forethrusts develop at the toe of the wedge, in front of the previous fault, while backthrusts develop behind the toe of the wedge.

4.2. Force (ΔF) and distance (L) measurements

Force measurements for a typical CV32 experiment are shown in Fig. 4. The changes in measured force along the moving wall in these experiments resemble force measurements from other dry sand analog models (Nieuwland et al., 2001; Cruz et al., 2010; Souloumiac et al., 2012). Prior to formation of the first forethrust–backthrust pair, force increases as the moving wall makes contact with the foam block and the strain gauges are loaded, shown by the linearly increasing segment of the force curve starting at 7 mm of backwall displacement in Fig. 4. The elastic loading occurs within ∼1 mm of displacement. The subsequent non-linear force evolution is due to slip on the detachment and diffuse compaction within the sand pack (region D in Fig. 4) (Bernard et al., 2007). Then, force decreases sharply from a local peak to a trough with the initial and each subsequent episode of fault growth (Fig. 4). Between faulting episodes, the force increases as the wedge grows in height and length.

At the start of these experiments, a force drop does not accompany slip along the detachment, which occurs prior to ramp fault development. This slip is observed from the PIV analysis, and is associated with horizontal compaction of the sand pack prior to ramp development. The lack of a drop in force at the time of detachment slip propagation is due to the non-softening character of slip along the glass/sand interface at the base of the sandbox. Indeed, the rigidity of the glass surface does not require grain re-

arrangements to allow for slip. Consequently, slip along this surface may not reduce the compliance of the system, and so may not result in a drop in force along the moving wall.

Generally, forethrust–backthrust pairs produce the largest decrease in backwall force because they have the largest fault area (Fig. 4). The average force drop recorded for pairs in CV32 is 1.5 ± 1.7 N, compared to 0.8 ± 0.6 N for backthrusts and 1.3 ± 0.8 N for forethrusts. The large error for each fault type stems from the wide range of fault areas within different thicknesses of sand pack. For each experiment, force data show low-amplitude, high frequency oscillations (0.1–0.4 N) due to instrument sensitivity and imperfections in set-up conditions. Instrument noise is eliminated by a 5-point moving average (0.5 s time averaging widow) of the force data, which is well below the timing of force variations of interest.

The average backwall displacement, L, over which these force drops occur in CV32 is 3.0 ± 1.2 mm. This is in good agreement with previous estimates of slip weakening distance for CV32 sand of 3 mm from ring-shear experiments (Klinkmüller et al., 2008) and of 2.4 mm from Casagrande shear experiments (Maillot, 2013). Error in the estimates of L from the sandbox experiments arises from the multiple local maxima/minima in the force data. A larger than 5-point moving average filter helps to identify a single, unique location for both the force peak and trough of each faulting event. This filter varies in size (20- to 60-point) according to the backwall displacement speed and the sand pack thickness for each experiment. The difference in backwall displacement from force peak to trough, between the handpicked values and the moving average values, gives the error of the displacement associated with a faulting event (0.1–1.4 mm).

4.3. Measurements of W_{prop} from force drops associated with faulting

The growth of thrusts ahead of the existing active faults involves slip both along the ramps and the basal detachment. As noted previously, no force drop accompanies slip along the detachment; however, increasing detachment length requires increasing force as the moving wall translates or compacts greater volume of material. Contraction of the sand pack due to detachment growth both consumes work and strengthens the sand pack, which ultimately transmits stress (and faulting) further outboard (Morgan, 2015). We can use the force data to differentiate the work required for the formation of ramp and detachment faults. The contribution of ramp and detachment faults to measured changes in work along the backwall, ΔW_{wall}, is calculated through an inverse analysis of the following relationship:

$$\Delta W_{wall}(A_R + A_D) = W_{prop\text{-}R} A_R + W_{prop\text{-}D} A_D \quad (3)$$

where $W_{prop\text{-}R}$ is the work of fault growth for ramps, $W_{prop\text{-}D}$ is the work for detachments, A_R is new ramp area, and A_D is new detachment area, all known values. Thus, $W_{prop\text{-}R}$ and $W_{prop\text{-}D}$ are estimated using inverse analysis to find values consistent with the multiple observations of ΔW_{wall} (eq. (3)). The analysis yields values of the work of fault growth per unit fault area, W_{prop}/A for ramps and detachments in CV32 of 0.288 J/m^2 and -0.121 J/m^2, respectively. The result of -0.121 J/m^2 for detachment formation suggests that detachment fault growth contributes to the work of the system in the opposite sense of the ramp growth. While the system deforms more easily as ramps grow, deformation of the system requires greater forces as detachments grow because of their increased length.

Fig. 5 shows W_{prop} versus fault area, A, for the growth of each ramp fault delineated by different sand pack thickness. To calculate A, we measure the fault length along the sidewall and multiply by the width of the sandbox (28 cm). We assume that the faults have the same geometry throughout the sandbox because

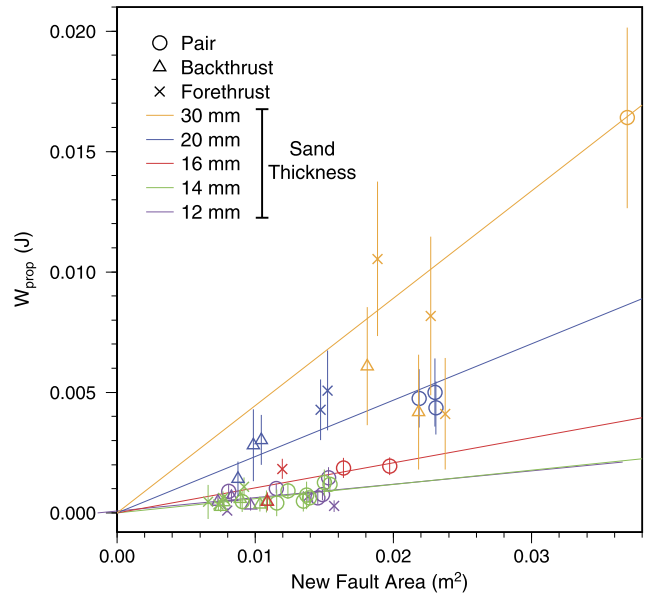

Fig. 5. W_{prop} versus new fault area for faults developed in the CV32 sand. Colors delineate data from different thickness sand packs. Slope of the best-fit line gives W_{prop}/A (J/m^2). The error bars are a combination of instrument noise and uncertainty associated with determining force drops. Increasing sand pack thickness consumes greater work to grow faults.

we observe faults developing across the entire sandbox, though deformation is documented along only one sidewall. Faults with larger A, which are associated with larger force drops, consume more W_{prop} than smaller faults. While we expect that thicker sand packs would have larger faults, comparable sized faults within different thickness sand packs consume different magnitudes of W_{prop}. Using a linear fit through each sand pack thickness, reveals that increasing sand pack thickness successively increases the steepness of the W_{prop}/A fit (Fig. 5). The 12 mm (0.056 ± 0.02 J/m^2) and 14 mm (0.059 ± 0.01 J/m^2) thicknesses have similar W_{prop}/A, while W_{prop}/A in the 16 mm (0.104 ± 0.06 J/m^2), 20 mm (0.234 ± 0.04 J/m^2) and 30 mm (0.358 ± 0.15 J/m^2) experiments are successively larger.

4.4. Comparison of W_{prop} estimates from the Casagrande shear box and the sandbox

Casagrande shear box tests performed by Maillot (2013) provide another direct measurement of W_{prop} for CV32 sand. The Casagrande shear box consists of a mobile lower half, which is displaced with a stepwise motor, and a fixed upper half, which is held in position by a force that is measured throughout the experiment. These experiments capture the evolution of shear force during fault slip for a range of normal stresses across the shear surface. W_{prop} is calculated from these changes in shear force, as shown in Fig. 1B, and the results are shown in Fig. 6A. W_{prop}/A ranges from 6 to 251 kPa and increases with normal compression across the fault. The applied normal loads on the Casagrande box far exceed those on faults within the contractional sandbox, which reach ~1.5 kPa for the thickest 30 mm sand pack tested here.

We compare W_{prop}/A estimates from the Casagrande shear box data with those from the sandbox data in Fig. 6B, which shows W_{prop}/A for all sandbox faulting events versus the normal compression at the time of faulting and the best-fit line from the shear box data in Fig. 6A. The normal compression is determined on planes representing incipient forethrusts and backthrusts dipping 30° and depends on both the lithostatic stress, σ_{vert}, and the horizontal compression due to the moving wall, σ_{hor}. σ_{hor} is estimated by reducing the horizontal force at the backwall by the sum of

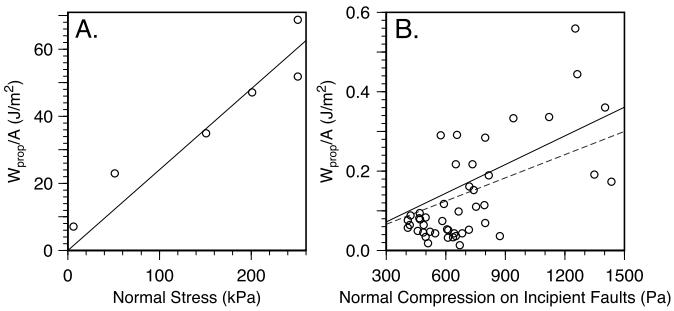

Fig. 6. A) W_{prop}/A calculated from Casagrande shear box experiments performed by Maillot (2013) for normal stresses across the fault from 6 to 251 kPa. Solid line shows best-fit through the data. B) Calculated W_{prop}/A for each faulting event at different normal compressive stress across incipient ramp faults at the base of the sand pack (dashed line shows best-fit). Estimated W_{prop}/A from Casagrande shear box data is shown again by the solid black line. The two datasets appear to have good match.

the resistive forces along the detachment. Both are calculated at the middle of the sand pack, representing the average over depth, as:

$$\sigma_{vert} = \rho g T/2 \tag{4a}$$

$$\sigma_{hor} = F/WT - \mu_d \rho g d \tag{4b}$$

Here, d is the position from the backwall, W is the width of the sandbox, T is the sand pack thickness, F is the total force on the moving wall, and μ_d is the frictional strength of the detachment, 0.265 determined by Cubas et al. (2010).

The magnitudes of normal compression in the Casagrande shear box experiments are much higher than those within the sandbox experiments, but the increase of W_{prop} with normal compression is consistent between the two datasets (Fig. 6B). The Casagrande shear box data yields the following relationship between W_{prop}/A (J/m^2) and normal compression, σ_n (Pa):

$$W_{prop}/A = 2.4 \times 10^{-4}\,(\mathrm{m})\,\sigma_n \tag{5}$$

and the sandbox data yields a similar relationship:

$$W_{prop}/A = 2.0 \times 10^{-4}\,(\mathrm{m})\,\sigma_n \tag{6}$$

The match between eq. (5) and eq. (6), found using two independent data sets, demonstrates the robustness of the finding that the work required to grow faults in granular material increases with depth. Outside of sandboxes that are specially adapted with strain gauges, force time series associated with faulting may not be readily available. Nevertheless, we can use evolution of shear strength data from direct shear tests for materials to determine the work required to grow faults.

4.5. Material comparison

To determine if W_{prop} depends on the sandbox material, in addition to normal compression, we analyze results for two additional experiments, with the finer-grained GA39 sand and with glass beads. Both materials have more rounded grains than CV32 sand (e.g. Panien et al., 2006), and more rounded grains may have lower static friction. In both experiments, drops in the backwall force concurrent with faulting are smaller than the sensitivity of the strain gauges, and therefore not detectable (Table 1, Fig. 7A). Faulting is evident in photographs of the side and top of the box, however, which allows for a qualitative comparison of the impact of the material on W_{prop}. We do this by comparing the timing and frequency of faulting for a given amount of backwall displacement in experiments with 14 mm thicknesses of GA39, glass beads, and

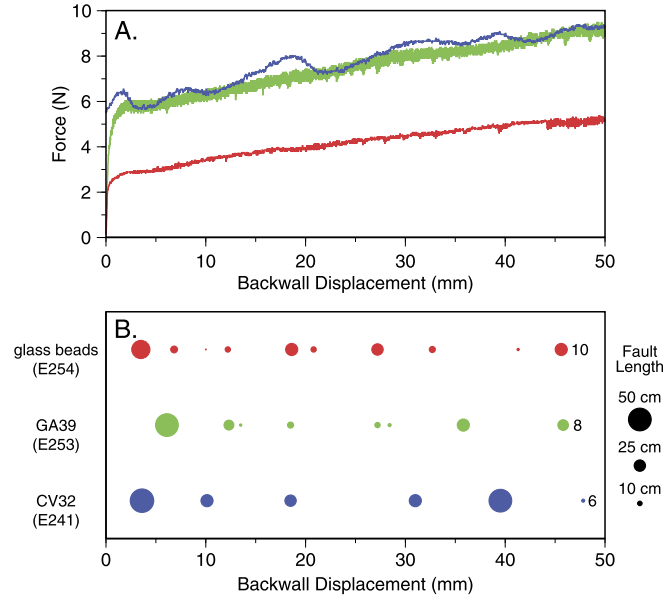

Fig. 7. A) Force displacement curves and B) timing of faulting during the first 50 mm of backwall displacement of CV32 (E241), GA39 (E253), and glass beads (E254) for 14 mm sand packs. Size of circles represents the total surface trace length of new faults (forethrust plus backthrust for forethrust–backthrust pairs). The lower work required to grow faults in finer/more rounded sand and glass beads is expressed as higher frequency and smaller length of growing faults. Larger faults develop within CV32 sand because the work required to grow faults is greater for CV32 sand than for glass beads of GA39 sand.

CV32 sand (Fig. 7B). Over the first 50 mm of backwall displacement, more faults develop in the experiment with glass beads (10 faults) than in the experiment with GA39 sand (8 faults) and the experiment with CV32 (6 faults) (Fig. 7B). More frequent faults have smaller slip than less frequent, larger slip faults, which require greater W_{prop} (Fig. 7B).

W_{prop} is stored in the system as W_{int} prior to fault formation (i.e., strain energy density, Cooke and Madden, 2014 and references therein). Larger W_{prop} requires more backwall displacement between faulting events because more W_{int} must accrue in order for the ΔW_{ext} due to growth of the new fault to meet the cost of growing the fault, W_{prop}; the system needs to accumulate more W_{int} to afford to grow the new fault. Consequently, comparing the timing of faulting and fault trace lengths measured in map view reveals the relative magnitudes of W_{prop} for these three materials. Under similar loading conditions, the more frequent and smaller faults that develop in GA39 and glass beads, relative to the CV32 experiments, reveal that faulting in these materials requires less work than in CV32, so W_{prop} is smaller.

Cubas et al. (2008) use limit analysis to show that, in addition to lower friction values due to slip weakening along ramp thrusts, an increase in friction along the detachment promotes fault duration. This analysis supports the result of more, short-lived faults within the glass beads, as the coefficient of friction along the detachment is lowest for glass beads (e.g. Panien et al., 2006). In contrast, the fewer, longer faults in experiments with CV32 sand reveal higher W_{prop} values. Thus, W_{prop} is influenced by material properties, in addition to normal compression.

5. Comparison and application of W_{prop} to crustal faulting

For analog experiments that are five orders of magnitude smaller than the crust to correctly simulate crustal deformation, the strength of the analog materials needs to be five orders of magnitude smaller than the strength of the crustal material (e.g. Hubbert, 1937). W_{prop}/A estimates from the sandbox experiments

with sand thickness ranging from 12 to 30 mm range from 0.06 to 0.36 J/m^2. These are five to seven orders of magnitude smaller than both laboratory (e.g., Wong, 1982; Ohnaka et al., 1997; Cox and Scholz, 1988; Kato et al., 2003) and field (e.g., Olgaard and Brace, 1983; Chester et al., 2005; Wilson et al., 2005; Pittarello et al., 2008) estimates, which range from 10^1 to 10^6 J/m^2, which follows proper scaling relations. However, these latter estimates do not take into account the dependency of the work of fault growth on normal compression, defining fault surface energy strictly as a material property.

The normal compression dependency of the work consumed by faults observed in the analog experiments implies a depth dependency of the work consumed during crustal fault growth. Faults that nucleate at deeper depths have to overcome larger normal compression in order to initiate slip. In this case, deeper faulting may yield larger stress drops. Even though this may be more pronounced for new fault development rather than for slip along existing faults, some earthquake catalogs show increased stress drop with depth (Baltay, 2014). Because other factors contribute to variations in stress drop (e.g., Baltay et al., 2011), this relationship is not evident in all catalogs.

The higher cost of developing new faults at greater depths may encourage continued slip along more unfavorably oriented structures at depth. At shallower depths, where W_{prop} is smaller, new faults that are more favorably oriented to the evolving stress field will be able to grow more easily. This also suggests that deeper faults may persist for longer than shallow faults. Consequently, within fault systems that experienced transitions in tectonic loading, such as inversion of a previously extensional terrain, fault geometry may differ with depth.

Fault slip will continue on an unfavorably oriented surface until there is energy enough to grow a new, more favorably oriented fault surface. Cooke and Madden (2014) demonstrate that, when the stresses meet the empirically derived strength measurements, the energy required for growth is equivalent to the energy available for growth. Consequently, fault growth can be predicted by knowing values for W_{prop} based on shear strength data (Cooke and Madden, 2014).

6. Conclusions

Data from contractional sandbox experiments and direct shear tests show that the work consumed by faulting in granular materials depends on normal compression. Faulting within thicker sand packs requires larger W_{prop}, the measure of work done between fault initiation and the fully weakened state, than faults of comparable size in thinner sand packs. We use force measurements within the sandbox experiments and shear strength data from Casagrande shear box tests on the CV32 sand to measure the work required to grow faults. Within analog sandbox experiments W_{prop} (J/m^2) $= 2.0 \times 10^{-4}$ (m) σ_n (Pa) and within the Casagrande shear box W_{prop} (J/m^2) $= 2.4 \times 10^{-4}$ (m) σ_n (Pa). The similarity between these independent data sets confirms this analysis. W_{prop} increases with higher normal compression, which suggests that the work required to grow faults is not just a material property, but also depends on depth and loading within the crust. However, sandbox experiments with different materials (GA39 sand and glass beads) reveal that materials affect W_{prop}. More rounded grains result in shorter time between faulting events and smaller faults, suggesting lower W_{prop}. Constraints on W_{prop} in rock can facilitate prediction of fault growth path and timing, which may differ at shallow and deep levels within the brittle crust due the dependence of W_{prop} on normal compression.

Acknowledgements

This research was supported by NSF grant EAR-1019747 to Cooke. The work was greatly improved by the careful reviews of George Hilley and Julia Morgan. PIV analysis was conducted using PIVlab for Matlab, developed by William Thielicke and Eize Stamhuis and available for download at http://pivlab.blogspot.com. Figs. 3–7 were made with Generic Mapping Tools (Wessel and Smith, 1998).

References

Adam, J., Urai, J.L., Wieneke, B., Oncken, O., Pfeiffer, K., Kukowski, N., Lohrmann, J., Hoth, S., van der Zee, W., Schmatz, J., 2005. Shear localisation and strain distribution during tectonic faulting—new insights from granular-flow experiments and high-resolution optical image correlation techniques. J. Struct. Geol. 27, 283–301. http://dx.doi.org/10.1016/j.jsg.2004.08.008.

Baltay, A., 2014. Stress drop and its relationship to radiated energy, ground motion and uncertainty. In: AGU Fall Meeting. S51D-08.

Baltay, A., Ide, S., Prieto, G., Beroza, G., 2011. Variability in earthquake stress drop and apparent stress. Geophys. Res. Lett. 38 (6). http://dx.doi.org/10.1029/2011GL046698.

Bernard, S., Avouac, J.-P., Dominquez, S., Simoes, M., 2007. Kinematics of fault-related folding from a sandbox experiment. J. Geophys. Res. 112, B03S12. http://dx.doi.org/10.1029/2005JB004149.

Brace, W.F., Walsh, J.B., 1962. Some direct measurements of the surface energy of quartz and orthoclase. Am. Mineral. 47, 1111–1122.

Chester, J.S., Chester, F.M., Kronenberg, A.K., 2005. Fracture surface energy of the Punchbowl fault, San Andreas system. Nature 437. http://dx.doi.org/10.1038/nature03942.

Cooke, M.L., Madden, E.H., 2014. Is the Earth lazy? A review of work minimization in fault evolution. J. Struct. Geol. 66, 334–346. http://dx.doi.org/10.1016/j.jsg.2014.05.004.

Cooke, M.L., Murphy, S., 2004. Assessing the work budget and efficiency of fault systems using mechanical models. J. Geophys. Res. 109, B10408. http://dx.doi.org/10.1029/2004JB002968.

Cox, S.J.D., Scholz, C.H., 1988. On the formation and growth of faults, an experimental study. J. Struct. Geol. 10, 413–430. http://dx.doi.org/10.1016/0191-8141(88)90019-3.

Cruz, L., Malinski, J., Wilson, A., Take, W.A., Hilley, G., 2010. Erosional control of the kinematics and geometry of fold-and-thrust belts imaged in a physical and numerical sandbox. J. Geophys. Res. 115 (B09404), 1–15. http://dx.doi.org/10.1029/2010JB007472.

Cubas, N., Barnes, C., Maillot, B., 2013. Inverse method applied to a sand wedge: estimation of friction parameters and uncertainty analysis. J. Struct. Geol. 55, 101–113. http://dx.doi.org/10.1016/j.jsg.2013.07.003.

Cubas, N., Leroy, Y.M., Maillot, B., 2008. Prediction of thrusting sequences in accretionary wedges. J. Geophys. Res. 113, B12412. http://dx.doi.org/10.1029/2008JB005717.

Cubas, N., Maillot, B., Barnes, C., 2010. Statistical analysis of an experimental compressional sand wedge. J. Struct. Geol. 32, 818–831. http://dx.doi.org/10.1016/j.jsg.2010.05.010.

Del Castello, M., Cooke, M.L., 2007. Underthrusting-accretion cycle: work budget as revealed by the boundary element method. J. Geophys. Res. 113 (B12404), 1–14. http://dx.doi.org/10.1029/2007JB004997.

Dempsey, D., Ellis, S., Archer, R., Rowland, J., 2012. Energetics of normal faults earthquakes on dip slip faults. Geology 40, 279–282. http://dx.doi.org/10.1130/G32643.1.

Graveleau, F., Malavielle, J., Dominquez, S., 2012. Experimental modelling of orogenic wedges: a review. Tectonophysics 538–540, 1–66. http://dx.doi.org/10.1016/j.tecto.2012.01.027.

Griffith, A.A., 1920. The phenomena of rupture and flow in solids. Philos. Trans. R. Soc. Lond. 221, 163–198.

Hall, J., 1815. On the vertical position and convolutions of certain strata and their relationship with granite. Trans. R. Soc. Edinb. 7, 79–108.

Hardy, S., Duncan, C., Masek, J., Brown, D., 1998. Minimum work, fault activity and the growth of critical wedges in fold and thrust belts. Basin Res. 10, 365–373. http://dx.doi.org/10.1046/j.1365-2117.1998.00073.x.

Hoth, S., 2005. Deformation, erosion, and natural resources in continental collision zones – insight from scaled sandbox simulations. PhD thesis. GeoForschungsZentrum Potsdam, Potsdam, Germany. 141 pp.

Hubbert, M.K., 1937. Theory of scale models as applied to the study of geologic structures. Geol. Soc. Am. Bull. 48, 1459–1520.

Irwin, G.R., 1958. Fracture. In: Flugge, S. (Ed.), Handbuch der Physik. Springer-Verlag, Berlin, pp. 551–590.

Jaeger, J.C., Cook, N.G.W., Zimmerman, R.W., 2007. Fundamentals of Rock Mechanics, 4th ed. Blackwell Publishing, Malden, MA. 513 pp.

Kato, A., Ohnaka, M., Mochizuki, H., 2003. Constitutive properties for the shear failure of intact granite in seismogenic environments. J. Geophys. Res. 108 (B12060), 14:1–14:10. http://dx.doi.org/10.1029/2001JB000791.

Klinkmüller, M., Rosenau, M., Boutelier, D., Kemnitz, H., Schreurs, G., 2008. Properties benchmark of granular and viscous analogue materials. Boll. Geophys. 49, extended abstract, GeoMod2008, Florence, Italy.

Krantz, R.W., 1991. Measurements of friction coefficients and cohesion for faulting and fault reactivation in laboratory models using sand and sand mixtures. Tectonophysics 188 (1–2), 203–207. http://dx.doi.org/10.1016/0040-1951(91)90323-K.

Lohrmann, J., Kukowski, N., Adam, J., Oncken, O., 2003. The impact of analogue material properties on the geometry, kinematics, and dynamics of convergent sand wedges. J. Struct. Geol. 25, 1691–1711. http://dx.doi.org/10.1016/S0191-8141(03)00005-1.

Maillot, B., 2013. A sedimentation device to produce uniform sand packs. Tectonophysics 593, 85–94. http://dx.doi.org/10.1016/j.tecto.2013.02.028.

Masek, J.G., Duncan, C.C., 1998. Minimum-work mountain building. J. Geophys. Res. 103 (B1), 907–917. http://dx.doi.org/10.1029/97JB03213.

Morgan, J.K., 2015. Effects of cohesion on the structural and mechanical evolution of fold and thrust belts and contractional wedges: discrete element simulations. J. Geophys. Res. 120, 3870–3896. http://dx.doi.org/10.1002/2014JB011455.

Nieuwland, D.A., Urai, J.L., Knoop, M., 2001. In-situ stress measurements in model experiments of tectonic faulting. In: Lehner, F.K., Urai, J.L. (Eds.), Aspects of Tectonic Faulting. Springer-Verlag, pp. 155–167.

Ohnaka, M., Akatsu, M., Mochizuki, H., Odera, A., Tagashira, F., Yamamoto, Y., 1997. A constitutive law for the shear failure of rock under lithospheric conditions. Tectonophysics 277, 1–27. http://dx.doi.org/10.1016/S0040-1951(97)00075-9.

Olgaard, D., Brace, W.F., 1983. The microstructure of gouge from a mining-induced seismic shear zone. Int. J. Rock Mech. Min. Sci. Geomech. Abstr. 20 (1), 11–19. http://dx.doi.org/10.1016/0148-9062(83)91610-8.

Panien, M., Schreurs, G., Pfiffner, A., 2006. Mechanical behavior of granular materials used in analogue modelling: insights from grain characterization, ring-shear tests and analogue experiments. J. Struct. Geol. 28, 1710–1724. http://dx.doi.org/10.1016/j.jsg.2006.05.004.

Pittarello, L., Di Toro, G., Bizzarri, A., Pennacchioni, G., Hadizadeh, J., Cocco, M., 2008. Energy partitioning during seismic slip in pseudotachylyte-bearing faults (Gole Larghe Fault, Adamello, Italy). Earth Planet. Sci. Lett. 269, 131–137. http://dx.doi.org/10.1016/j.epsl.2008.01.052.

Savage, H., Cooke, M.L., 2010. Unlocking the effects of friction on fault damage zones. J. Struct. Geol. 32, 1732–1741. http://dx.doi.org/10.1016/j.jsg.2009.08.014.

Souloumiac, P., Maillot, B., Leroy, Y.M., 2012. Bias due to side wall friction in sand box experiments. J. Struct. Geol. 35, 90–101. http://dx.doi.org/10.1016/j.jsg.2011.11.002.

Wessel, P., Smith, W.H.F., 1998. New, improved version of the generic mapping tools released. Eos Trans. AGU 79 (47), 579. http://dx.doi.org/10.1029/98EO00426.

Wilson, B., Dewers, T., Reches, Z., Brune, J., 2005. Particle size and energetics of gouge from earthquake rupture zones. Nature 434, 749–752. http://dx.doi.org/10.1038/nature03433.

Wong, T.-F., 1982. Shear fracture energy of Westerly granite from post-failure behavior. J. Geophys. Res. 87 (B2), 990–1000. http://dx.doi.org/10.1029/JB087iB02p00990.

Yagupsky, D.L., Brooks, B.A., Whipple, K.X., Duncan, C.C., Bevis, M., 2014. Distribution of active faulting along orogenic wedges: minimum-work models and natural analogue. J. Struct. Geol. 66, 90–101. http://dx.doi.org/10.1016/j.jsg.2014.05.025.